Report 72-1

August 1972

AN INVESTIGATION INTO THE ENERGETICS OF SEVERE LOCAL STORMS USING A TWO-DIMENSIONAL NUMERICAL MODEL

By: R. E. Schlesinger

Prepared for:

National Science Foundation

Grant No. GI-31278X

C. E. Anderson, Principal Investigator

Department of Meteorology
University of Wisconsin
Madison, Wisconsin 53706

REVISED ERRATA SHEET

(To be substituted for previous errata sheet)

Report 72-1 August 1972

Page 1, line 8: "Frankhauser" should read "Fankhauser".

Page 6: The last term of equation (6) should read

$$\frac{c_p \rho_0}{L_{vw}} (\gamma_d - \Gamma) w$$

Page 8: Equations (8)-(14) should read as follows:

$$K_M = \left\langle \frac{\bar{u}^2}{2} \right\rangle \tag{8}$$

$$K_E = \left\langle \frac{u'^2 + w'^2}{2} \right\rangle \tag{9}$$

$$P_M^* = -\langle \Phi \rangle \left\langle \frac{\hat{T}}{T_0} + k\hat{q}_v \right\rangle \tag{10}$$

$$P_E^* = -\left\langle \Phi'' \left(\frac{\hat{T}}{T_0} + k\hat{q}_v \right) \right\rangle \tag{11}$$

$$P_W = \langle L\Phi/\rho_0 \rangle \tag{12}$$

$$H_L = \langle L_{vw} q_v \rangle \tag{13}$$

$$H_S = \langle c_p T \rangle \tag{14}$$

Page 22: Along the ordinate, Z(km), of the bottom-most diagram of Figure 4, the numeral 0 above the 5 should read 10.

Page 35: The expression $P_M^*/\partial t$ in the left margin midway through Table 3 should read $\partial P_M^*/\partial t$.

Page 40, lines 2 and 3: "The dominance of boundary work (B_2) in decreasing the mean kinetic energy..." should read "The dominance of boundary work (B_2) in changing the mean kinetic energy".

(On the previous errata sheet, minus signs in equations (10) and (11) were missing, and the error on page 40 was not listed.)

Report 72-1 August 1972

AN INVESTIGATION INTO THE ENERGETICS OF SEVERE LOCAL STORMS USING A TWO-DIMENSIONAL NUMERICAL MODEL

By: R. E. Schlesinger

Prepared for:

National Science Foundation Grant No. GI-31278X

C. E. Anderson, Principal Investigator

Department of Meteorology
University of Wisconsin
Madison, Wisconsin 53706

TABLE OF CONTENTS

LIST OF FIGURES

1. INTRODUCTION

In contrast to the relatively short-lived and often multi-cellular air-mass thunderstorms studied by Byers and Braham (1949) in the Thunderstorm Project, some large severe thunderstorms have been observed to have a quasi-steady mature state lasting 30 minutes to two hours or longer, possibly as single "supercells". A number of schematic models have been proposed by Browning and Donaldson (1963), Newton and Newton (1959), Goldman (1968) and Frankhauser (1971) in attempts to explain this persistence in an environment characterized by considerable vertical wind shear, an element which has long been observed to suppress development of shallow cumulus and which was regarded by Byers and Braham (1949) as unfavorable to thunderstorm development.

These schematic models have emphasized, in general terms, the efficiency of large persistent thunderstorms as thermodynamic engines. At an earlier data, Normand (1946) briefly noted that an upshear-tilted updraft coexisting with a downshear-tilted downdraft upshear of it should contribute to the kinetic energy of the disturbance.

However, even today few attempts have been made to study in detail the ways in which individual physical processes contribute to specific types of energy changes within, and in the surroundings of, severe convective storms.

To examine with satisfactory accuracy the time variations of kinetic, potential, sensible and latent heat energies of air, a detailed knowledge of temperature, pressure, mixing ratio and liquid water content in and near a storm is required. The aircraft and dropsonde observations planned in the National Hail Research Experiment should make possible better coverage of this sort than has previously been possible. Without such detailed observations, perhaps the best theoretical tool for attempting to closely analyze storm energetics is a two- or three-dimensional numerical model.

Asai (1964) studied mean and eddy kinetic and potential energy variations in a two-dimensional moist convection model. However, this model simulated shallow non-precipitating cumulus. Liquid water drag, probably important to the energetics of precipitating cumulonimbus, was absent in view of the assumption that any liquid water disappeared from the system upon condensation. In a two-dimensional model of precipitating cumulonimbus, Takeda (1966) analyzed the time changes of several energies, but computations were terminated after only 15 minutes of simulated time because unrealistic feedback developed from the periodic

lateral boundary conditions which were assumed. Also, Takeda's initial conditions were questionable, prescribing a deep cloud with no vertical motion and almost no temperature disturbance. Time variations of kinetic and potential energy for air were considered in the early squall line model of Ogura and Charney (1962) and in three-dimensional deep convection modeling by Shafrir et al. (1970); however, this was done mainly as a check upon the accuracy of the numerical schemes used in these models. Base states with no ambient wind were assumed in order to have simple energy conservation laws that would not be expected to hold, however, in a sheared open region of the sort in which actual severe thunderstorms often develop.

In the above context, the balance of this report will summarize an analysis of the time variation for several energy transformation rates from the cumulus state to the peak of the mature stage in a two-dimensional numerical model of sheared precipitating cumulonimbus (Schlesinger, 1972). The reference just mentioned covers in detail the use of this model for studying the combined influence of two initial parameters, low-level moisture supply and mid-tropospheric vertical wind shear, upon the evolution of convection. A shallow cloud with a weak circulation is assumed initially present, and aperiodic open lateral boundaries are used. The run performed in April 1972 for

analysis of energetics disregards friction and includes minor changes in boundary conditions as well as refinements in the method for estimating pressure perturbations, but is otherwise the same as the case of intermediate moisture supply and moderate shear describe in the above reference.

2. THE MODEL

a) Main assumptions

The chief assumptions incorporatedinto the numerical model are the following:

1) Flow is two-dimensional in an x-z plane, i.e., v is zero and $\partial Q/\partial y$ is zero for each variable Q.

2) The Coriolis force is neglected.

3) The drag force exerted by liquid water is equal to its weight.

4) Motions are anelastic, i.e., local time changes of air density are neglected in the continuity equation.

5) Variation of specific heat of air at constant pressure or of the latent heat of vaporization is neglected.

6) Pressure deviations are important to gravitational buoyancy but not to parcel temperature changes.

7) Any supersaturation is removed through instantaneous release of latent heat, and any liquid water in unsaturated air evaporates instantaneously until the wet-bulb temperature is reached or all liquid water is consumed.

8) Saturated ascent and descent are moist-adiabatic.

9) All water drops have the same horizontal velocity components as the air.

10) Liquid water is partitioned into cloud droplets and precipitation by the parameterization method of Takeda (1965, 1966) following use of the static adjustment of

assumption 7 wherever needed.

11) Explicit friction or diffusion is not included.

The above assumptions are covered in detail elsewhere (Schlesinger, 1972). The last assumption represents a slight change from previously, when friction at points on or in the cloud was included using a formulation of Lettau (1967) for free turbulence. Analysis of individual forces revealed that the friction was one to two orders of magnitude smaller than the other forces; removing it from the model turned out to have negligible effect on the evolution or intensity of convection.

For completeness, using symbols defined in Appendix A, the governing equations for the model are listed below:

$$\frac{\partial u}{\partial t} = - u \frac{\partial u}{\partial x} - w \frac{\partial u}{\partial z} - \frac{1}{\rho_0} \frac{\partial \hat{p}}{\partial x} \tag{1}$$

$$\frac{\partial w}{\partial t} = - u \frac{\partial w}{\partial x} - w \frac{\partial w}{\partial z} - \frac{1}{\rho_0} \frac{\partial \hat{p}}{\partial z} + g\left(\frac{\hat{T}}{T_0} + k\hat{q}_v - \frac{\hat{p}}{p_0} - \frac{L}{\rho_0}\right) \tag{2}$$

$$\frac{\partial (\rho_0 u)}{\partial x} + \frac{\partial (\rho_0 w)}{\partial z} = 0 \tag{3}$$

$$\frac{\partial T}{\partial t} = - u \frac{\partial T}{\partial x} - w\left(\frac{\partial T}{\partial z} + \Gamma\right) \tag{4}$$

$$\frac{\partial q_v}{\partial t} = - u \frac{\partial q_v}{\partial x} - w \frac{\partial q_v}{\partial z} - \frac{c_p}{L_{vw}} (\gamma_d - \Gamma) w \tag{5}$$

$$\frac{\partial L}{\partial t} = - u \frac{\partial L}{\partial x} - w \frac{\partial L}{\partial z} + \frac{\partial}{\partial z} (V L_p) + \frac{wL}{\rho_0} \frac{\partial \rho_0}{\partial z} + \frac{c_p}{L_{vw}} (\gamma_d - \Gamma) w \tag{6}$$

In the actual integration procedure, the velocity components are defined in terms of a stream function ψ,

$$\rho_0 u = \partial\psi/\partial z \qquad (7\text{-a})$$

$$\rho_0 w = -\partial\psi/\partial x \qquad (7\text{-b})$$

and a vorticity equation similar to that of Takeda (1971) is used instead of the primitive equations (1) and (2), the stream function then being obtained from the vorticity by Liebmann overrelaxation. The term $-g\hat{p}/p_0$ in (2), representing the contribution of pressure perturbations to the buoyancy, was neglected by Takeda and most other cloud modelers. However, this term may be important in deep clouds, as emphasized by Barnes (1970). This term appears differentiated with respect to x in the vorticity equation, and can then be evaluated by substitution for $\partial\hat{p}/\partial x$ using (1). The recovery of $\hat{p}$ itself is complicated by the fact, stressed by Ogura and Charney (1962), that an infinite set of solutions satisfying the equations of motion exists under the most consistent physical boundary conditions at top and bottom. In Appendix B, the main steps are sketched for the method used in the present study for obtaining a particular pressure solution whereby unreasonably high or low values of $\hat{p}$ might be avoided.

b) Energy equations

The following definitions are used for the forms

of energy considered in this study, using symbols defined in Appendix A:

$$K_M = \frac{1}{XZ<\rho_0>} \int_0^X \int_0^Z \rho_0 \frac{\bar{u}^2}{2} \, dzdx \tag{8}$$

$$K_E = \frac{1}{XZ<\rho_0>} \int_0^X \int_0^Z \frac{u'^2+w'^2}{2} \, dzdx \tag{9}$$

$$P_M^* = \frac{-1}{XZ<\rho_0>} \int_0^X \int_0^Z \rho_0 <\Phi> (\frac{\hat{T}}{T_0} + k\hat{q}_v) dzdx \tag{10}$$

$$P_E^* = \frac{-1}{XZ<\rho_0>} \int_0^X \int_0^Z \rho_0 \Phi'' (\frac{\hat{T}}{T_0} + k\hat{q}_v) dzdx \tag{11}$$

$$P_W = \frac{1}{XZ<\rho_0>} \int_0^X \int_0^Z L\Phi dzdx \tag{12}$$

$$H_L = \frac{1}{XZ<\rho_0>} \int_0^X \int_0^Z \rho_0 L_{vw} q_v dzdx \tag{13}$$

$$H_S = \frac{1}{XZ<\rho_0>} \int_0^X \int_0^Z \rho_0 c_p T dzdx \tag{14}$$

The asterisks in P_M^* (mean potential energy of air) and P_E^* (eddy potential energy of air) are present in order to emphasize that the right-hand sides of (10) and (11) contain only two of three summands in the integrands. These integrands involve density changes, which are expressible in terms of temperature, mixing ratio and pressure perturbations; since the last of these three perturbations is not completely certain in view of the aforementioned non-

uniqueness, and the anelastic assumption does not admit a prognostic equation for $\hat{p}$, transformation rates for the full potential energy terms could not be reliably evaluated.

Equation (1)-(6) and (8)-(14) may then be used to obtain the following tendency equations for each of the energies, using two-dimensional integrals A_1 through A_{14} and lateral boundary integrals B_1 through B_9 whose mathematical forms and physical significance are given in Tables 1 and 2:

$$\partial K_M/\partial t = -A_1 + A_2 + B_1 + B_2 \tag{15}$$

$$\partial K_E/\partial t = A_3 + A_4 + A_5 - A_6 + A_1 + B_3 + B_4 \tag{16}$$

$$\partial P_M^*/\partial t = A_7 + A_9 + B_5 \tag{17}$$

$$\partial P_E^*/\partial t = A_8 + A_{10} - A_3 + B_6 \tag{18}$$

$$\partial P_W/\partial t = A_{11} + A_{12} + A_6 + B_7 \tag{19}$$

$$\partial H_L/\partial t = -A_{13} + B_8 \tag{20}$$

$$\partial H_S/\partial t = A_{14} + A_{13} + B_9 \tag{21}$$

Note in particular the presence of four conversion terms, appearing with opposite signs in pairs of equations: A_1 (conversion of mean to eddy kinetic energy by mean wind shear), A_3 (conversion of eddy potential to eddy kinetic energy by buoyancy forces), A_6 (conversion of eddy kinetic energy to potential energy of liquid water by the drag force which it exerts) and A_{13} (conversion of released latent

TABLE 1

Energy Integrals of Form $\dfrac{\int_0^X \int_0^Z \rho_0 Q\,dz\,dx}{\int_0^X \int_0^Z \rho_0\,dz\,dx}$

Term	Associated Quantity Q	Significance
A_1	$-u'w'\partial\bar{u}/\partial z$	Conversion of K_M to K_E by mean wind shear
A_2	$-\bar{u}\tilde{w}\ \partial\bar{u}/\partial z$	Change in K_E due to mean wind shear and net ascent or descent across region
A_3	$gw'(\frac{\hat{T}}{T_0} + k\hat{q}_v)$	Conversion of P_E^* to K_E by T- and q_v-buoyancy
A_4	$-gw'\hat{p}/p_0$	Change in K_E due to the pressure component of the buoyancy
A_5	$-w'\hat{p}(\partial\rho_0/\partial z)/\rho_0^2$	Change in K_E due to compressibility
A_6	$gw'L/\rho_0$	Conversion of K_E to P_W by liquid water drag
A_7	$w'\langle\Phi\rangle(S + k\partial q_{vo}/\partial z)$	Change in P_M^* due to conditional instability
A_8	$w'\Phi''(S + k\partial q_{vo}/\partial z)$	Change in P_E^* due to conditional instability
A_9	$\frac{c_p}{L_{vw}} kw'\langle\Phi\rangle(\gamma_d - \Gamma)$	Change in P_M^* due to latent heat release
A_{10}	$\frac{c_p}{L_{vw}} kw'\Phi''(\gamma_d - \Gamma)$	Change in P_E^* due to latent heat release
A_{11}	$-gL_p V/\rho_0$	Loss of P_W due to rainout

A_{12}	$\frac{c_p}{L_{vw}} w'\Phi(\gamma_d - \Gamma)$	Change in P_W due to latent heat release
A_{13}	$c_p w'(\gamma_d - \Gamma)$	Conversion of H_L to H_S by latent heat release
A_{14}	$-gw'$	Change in H_S due to incompletely compensated dry-adiabatic contributions in region

TABLE 2

Energy Integrals of Form $\left(\int_0^Z \rho_0 Q \Big|_{(0,z)}^{(X,z)} dz\right) / \left(\int_0^X \int_0^Z \rho_0 dz dx\right)$

Term	Associated Quantity Q	Significance
B_1	$-\bar{u}(u^2 + u'^2)/2$	Change in K_M due to boundary effects other than boundary work
B_2	$-\bar{u}\hat{p}/\rho_0$	Change in K_M due to boundary work
B_3	$-u(u'^2 + w'^2)/2$	Change in K_E due to boundary advection
B_4	$-u'\hat{p}/\rho_0$	Change in K_E due to boundary work
B_5	$u\langle\Phi\rangle(\frac{\hat{T}}{T_0} + k\hat{q}_v)$	Change in P^*_M due to boundary advection
B_6	$u\Phi''(\frac{\hat{T}}{T_0} + k\hat{q}_v)$	Change in P^*_E due to boundary advection
B_7	$-u\Phi L/\rho_0$	Change in P_W due to boundary advection
B_8	$-uL_{vw}q_v$	Change in H_L due to boundary advection
B_9	$-uc_pT$	Change in H_S due to boundary advection

heat to sensible heat). The relative importances of these terms will become apparent in Section 5 when the main results are summarized.

3. GRID DIMENSION AND INITIAL CONDITIONS

The computational grid, including dimensions and initial conditions, has been described in detail elsewhere (Schlesinger, 1972). Nevertheless, a fewsalient features to keep in mind within the present context are now pointed out.

A rectangular 55-by-21 grid is used, with grid separations of 3.2 km in the horizontal (total extent 172.8 km) and 700 m in the vertical (total depth 14 km). The initial base state is conditionally unstable up to about 8 km. Apart from a shallow stable layer between 9.1 and 10.5 km with a lapse rate about one-third the dry-adiabatic value, the temperature decreases upward at about three-fourths the dry-adiabatic rate. Relative humidity decreases sharply from 80% throughout the first 2.8 km to 25% at 4.2 km, and remains very low at all higher levels. Relative to the earth, the basic wind increases from 6 to 10 m sec^{-1} through the lowest 3.5 km and to 24 m sec^{-1} at 8.4 km, with no further shear at higher levels.

To keep the model cloud within the grid for a longer time than otherwise possible, the grid is shifted bodily downwind in a discrete fashion, one horizontal grid separation at a time, so that the leading edge of the cloud is never less than 12 grid separations (38.4 km) from the downwind boundary. Following the initial instant, at which

a shallow buoyant cloud with a weak convective circulation is assumed present, about 63 minutes of time are simulated for the energetics analysis. Grid translation starts at about 37 minutes, with 20 shifts at the end of the time interval in question. In order to examine energy tendencies in a region which is stationary relative to the earth, only the 35-by-21 subregion common to the initial and final domains is considered.

Apart from some minor changes which have little effect, boundary conditions are as described in the above reference.

4. EVOLUTION OF CONVECTION

a) Cloud growth with time

Figure 1 shows the successive outlines and positions of the model cloud, the full grid and the subregion relative to the earth at time intervals of approximately 9 minutes from the initial time to the latest time considered*. The cloud core moves approximately with the wind at 3 to 4 km. Growth of the cloud is slow during the precipitation-free stages (Figures 1-a through 1-c), but much more rapid after precipitation has developed (Figures 1-d and 1-e); at about 24 minutes, the cloud top first reaches the -20 C level, whereupon precipitation is assumed to commence according to the parametrization method of Takeda (1965, 1966) which is used to represent the role of ice crystals without explicit inclusion of the ice phase. Asymmetry due to ambient wind shear is marked at 27.5 minutes and at all later times. Continuous spreading of the anvil is apparent at and after 36.1 minutes (Figures 1-e through 1-h). Precipitation first reaches the surface at about 40 minutes; the small secondary cloud at low levels behind the trunk of the main cloud at the last two stages shown has formed for reasons to be noted shortly.

---

*Due to the use of a variable time step in the model, successive time intervals are not exactly equal, ranging from 8.6 to 9.5 minutes.

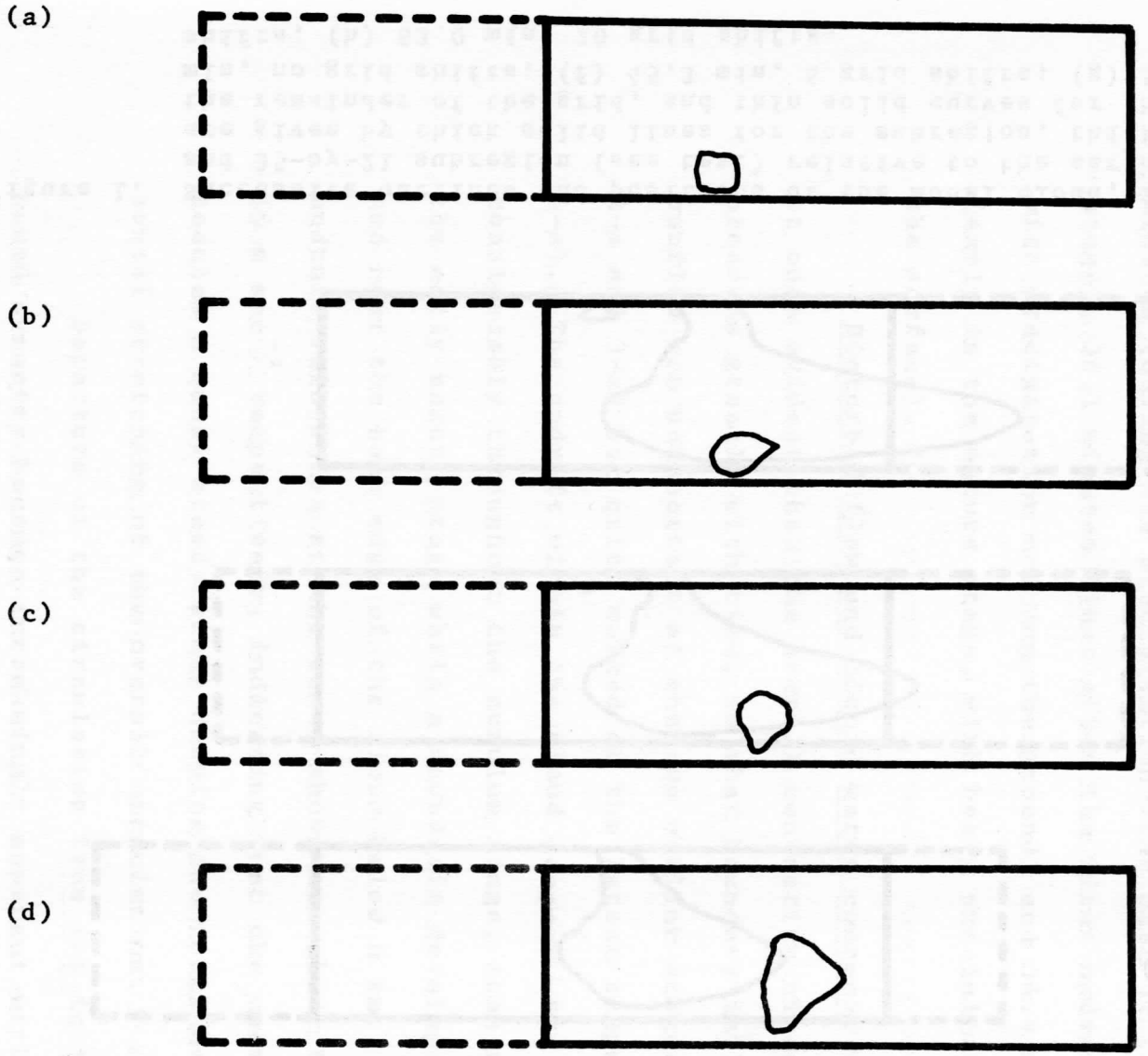

Figure 1. Successive outlines and positions of the model cloud, full 55-by-21 grid and 35-by-21 subregion (see text) relative to the earth's surface. Boundaries are given by thick solid lines for the subregion, thick dashed lines for the remainder of the grid, and thin solid curves for the cloud. (a) Initial time, no grid shifts; (b) 9.0 min, no grid shifts; (c) 18.5 min, no grid shifts; (d) 27.5 min, no grid shifts.

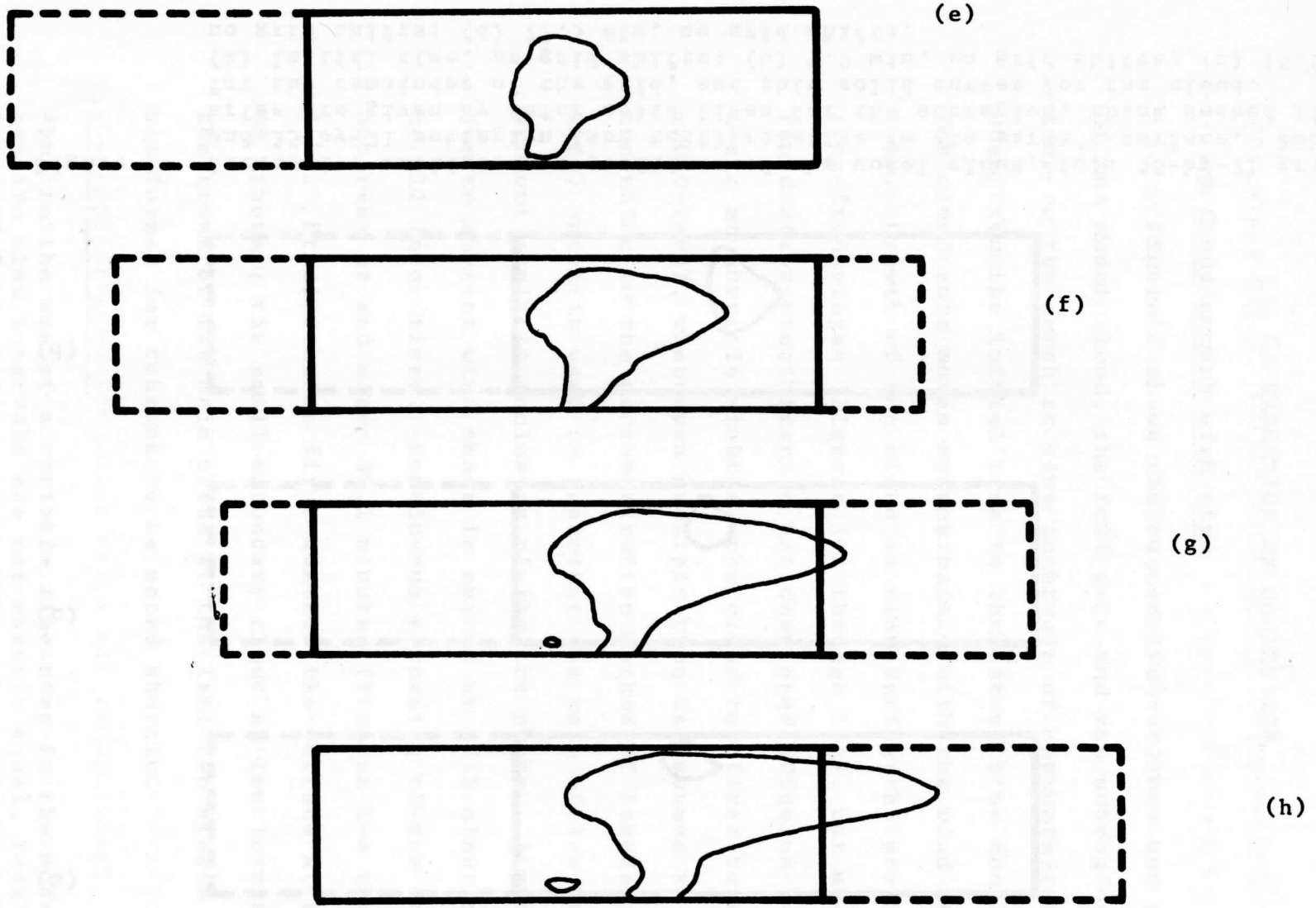

Figure 1. Successive outlines and positions of the model cloud, full 55-by21 grid and 35-by-21 subregion (see text) relative to the earth's surface. Boundaries are given by thick solid lines for the subregion, thick dashed lines for the remainder of the grid, and thin solid curves for the cloud. (e) 36.1 min, no grid shifts; (f) 45.3 min, 6 grid shifts; (g) 54.4 min, 14 grid shifts; (h) 63.0 min, 20 grid shifts.

b) Development of disturbance fields in the subregion

Figures 2 through 4 show the deviations of the airflow, temperature and pressure fields in the subregion at three different stages of convective development: at 18.5 minutes (during the precipitation-free part of the cumulus stage), 36.1 minutes (just after the first updraft peak, with precipitation nearing the ground) and 54.4 minutes (early in the mature stage, with heavy precipitation at the surface).

Disturbed flow and liquid water content. It is at once evident that the overall convective circulation broadens greatly with time, so that boundary inflow and outflow are unimportant at the two earlier stages (Figures 2-a and 3-a) but quite marked at the latest stage (Figure 4-a). The updraft within the cloud deepens and broadens considerably throughout the cumulus stage, then narrows during the early mature stage while a downdraft develops along and near the back edge of the cloud below 6 km. The maximum updraft velocities at the times shown are about 6, 11 and 10 m sec^{-1} respectively, indicating that the updraft core reaches a quasi-steady state despite the continuous horizontal stretching of the overall circulation.

Departure of the circulation from its initially assumed symmetry becomes increasingly apparent with time. The upshear branch is stronger than the downshear branch,

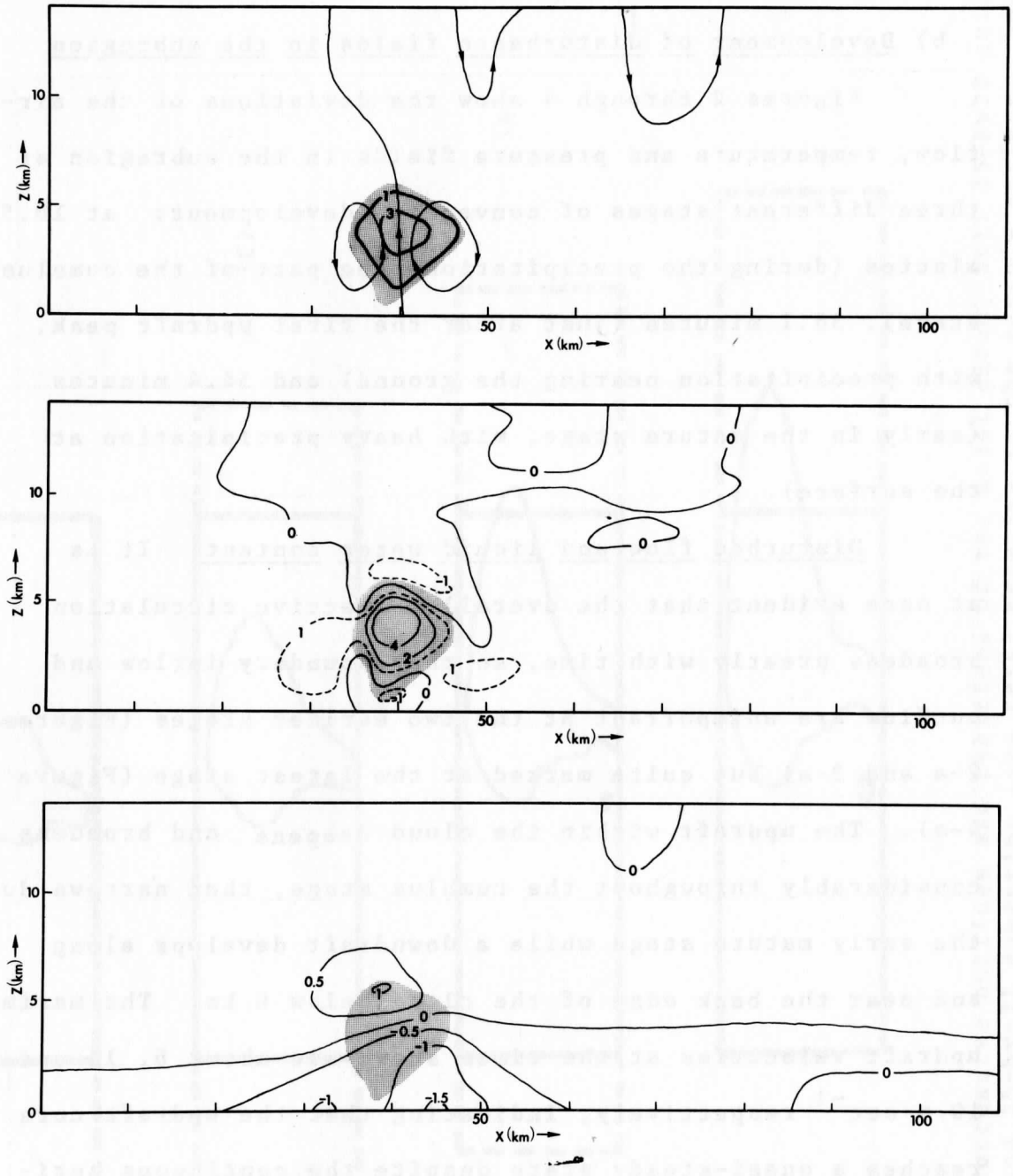

Figure 2. Convection in the 35-by-21 subregion after 18.5 min. In all three diagrams, the cloud is indicated by shading. (a) Deviation of stream function from base state, $\hat{\psi}$, and total liquid water content L; streamlines are thin solid curves with arrows, contoured at intervals of 10^7 gm m^{-1} sec^{-1}, and isolines of L (gm m^{-3}) are thick solid curves. (b) Deviation of temperature from base state, $\hat{T}$, in C. (c) Deviation of pressure from base state, $\hat{p}$, in mb.

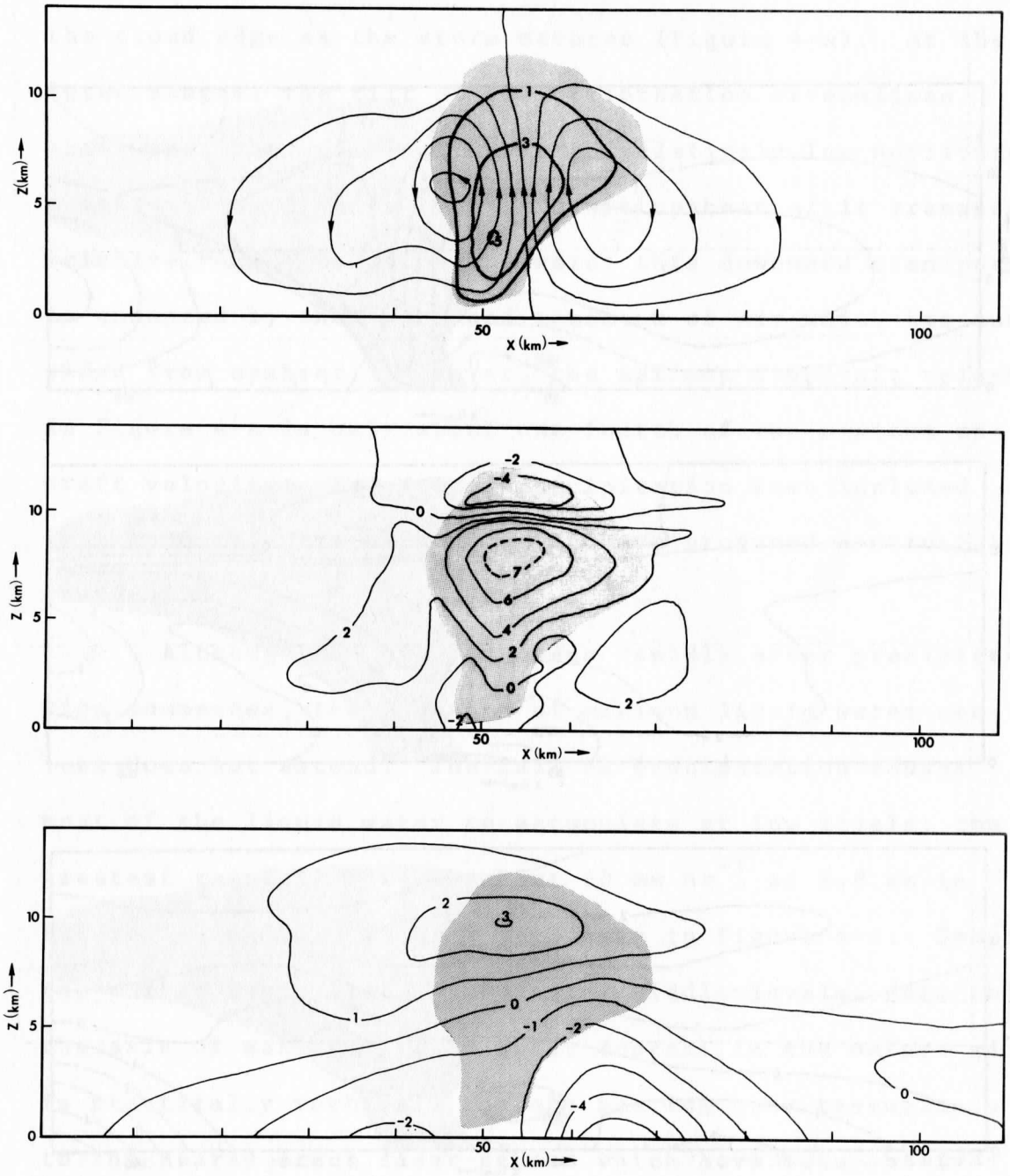

Figure 3. Same as Figure 2, but for 36.1 min.

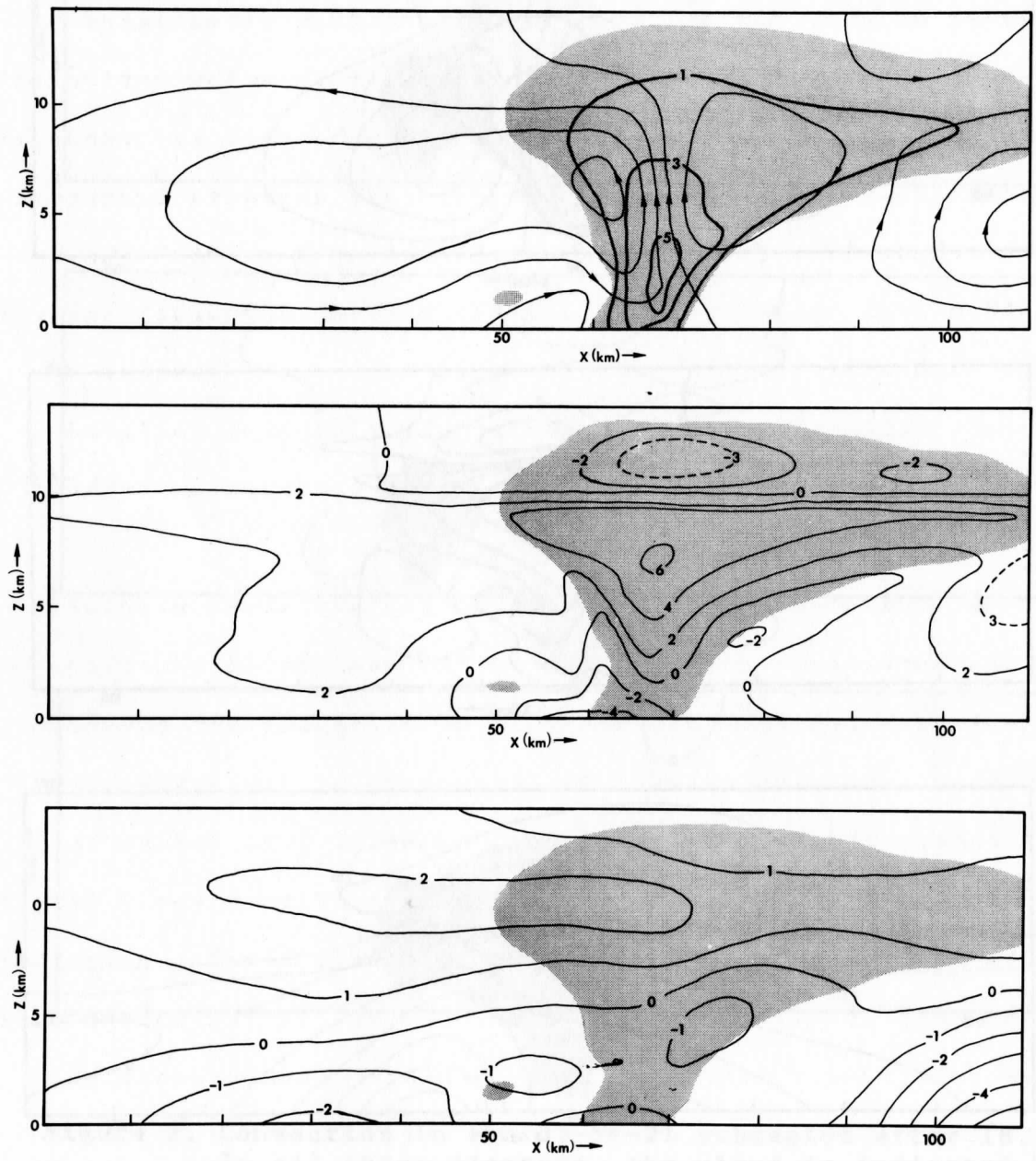

Figure 4. Same as Figure 2, but for 54.4 min.

and only the latter branch shows a marked splitting along the cloud edge as the storm matures (Figure 4-a). At the later stages, the tilt of the perturbation streamlines shows that the updraft transports relatively low horizontal momentum upward while the downdraft upshear of it transports relatively high momentum downward; this downward transport is enhanced by the increased momentum of air which has subsided from upshear. However, the maximum downdraft velocity in Figure 4-a is only about one-fourth of the maximum updraft velocity. Had frozen precipitation been included in the model, partial melt might have produced a stronger downdraft.

Although the cloud deepens rapidly after precipitation commences, the location of maximum liquid water content does not ascend. The fall of precipitation causes most of the liquid water to accumulate at low levels; the greatest rainfall rate is about 60 mm hr^{-1} at 2.8 km in Figure 3-a and 110 mm hr^{-1} at 1.4 km in Figure 4-a. Despite the marked basic wind shear in the middle levels, note that the axis of maximum liquid water content in the mature storm is practically vertical, thereby bearing some resemblance to the nearly erect radar echoes which have been observed in some severe thunderstorms in sheared surroundings. The small secondary cloud, with liquid water content considerably less than 1 gm m^{-3}, is induced by convergence

between low-level outflow from the storm and the inflow of air which has subsided in back of it.

Temperature. Release of latent heat produces pronounced local warming (up to 7°C) in the cloud core, while dry-adiabatic compensatory sinking produces smaller temperature rises (up to 3°C) outside the cloud. Below 6 km, evaporation at cloud edges produces cold tongues which become more developed with time. At 54.4 minutes (Figure 4-b), surface cooling of as much as 5°C behind the cloud core has resulted from evaporation of precipitation. Latent heat release in the uppermost parts of the cloud is insufficient to counteract cooling due to forced ascent which occurs as the cloud deepens. Packing of perturbation isotherms near 10 km (Figures 3-b and 4-b) results from ascent through the thin stable layer. Downshear of the storm core, the cold tongue between the two regions of strong warming is mainly responsible for the earlier-mentioned splitting of the updraft.

Pressure. On the whole, the pressure falls in the lower part of the convectively active region and rises in the upper part. Two centers of pressure deficit are present at low levels, the main one under the leading cloud edge and the secondary one behind the trailing edge. At 54.4 minutes (Figure 4-c), a well-marked shallow dome of relatively high pressure has developed in the cold air beneath

and just behind the storm core.

From an examination of the temperature and pressure disturbances at any one time, the role of temperature changes in producing hydrostatic contributions to pressure changes is apparent. As might be expected, the two surface pressure minimums are under the locations of greatest warming within the compensatory downdrafts. The minimum ahead of the storm core is the more pronounced partly because of the asymmetry of the upper-level warm outflow from the updraft; on the downshear side, both this upper warm current and the dry-adiabatic warming beneath it tend to lower the surface pressure, while on the upshear side the only dominant contribution comes from the dry-adiabatic warming. The "thunderstorm high" at the surface is largely a result of the evaporatively produced cooling. In the upper portion of the updraft, the pressure excess is partly due to the cooling near the cloud top, although it may also be in part analogous to the dynamic pressure excess which would result in a steady laminar jet as it diverges on approaching a rigid upper boundary (Barnes, 1970).

Through the lower half of the region, there is a slight net pressure increase from the upshear to the downshear boundary at 18.5 minutes (Figure 2-c), a small decrease at 36.1 minutes (Figure 3-c) and a very pronounced net decrease at 54.4 minutes (Figure 4-c). This will soon

be seen to be important in considering the effects of lateral boundary work upon mean and eddy kinetic energy tendencies.

5. RESULTS OF THE ENERGETICS ANALYSIS

a) Net energy transformation rates

In Figures 5 through 9, the net transformation rates for each of the energies defined in (8)-(14) are plotted as functions of time. Two curves are plotted for all energies except mean kinetic energy; the solid curve is obtained from the right-hand side of the associated equation among (15)-(21), while the dashed curve is obtained from the left-hand side. Systematic discrepancies between the two curves are due to the damping inherent in the numerical scheme used for advective terms in the model (forward in time, upstream in space). Apart from terms involving pressure perturbations (whose computation makes use of accelerations, as described in Appendix B), the right-hand sides of the transformation equations do not contain this damping, whereas the left-hand sides do. The pseudo-diffusive effect causes increases in eddy kinetic energy (Figure 5), liquid water potential energy (Figure 7) and sensible heat (Figure 9) to be underestimated by a factor of about two during the growth stage of the storm, and similarly for decreases in mean potential energy of air (Figure 6) and latent heat (Figure 8). However, the shapes and slopes of the two curves are quite similar at later times, indicating that the error due to numerical damping is quite straightforward in nature. Henceforth, all discussion

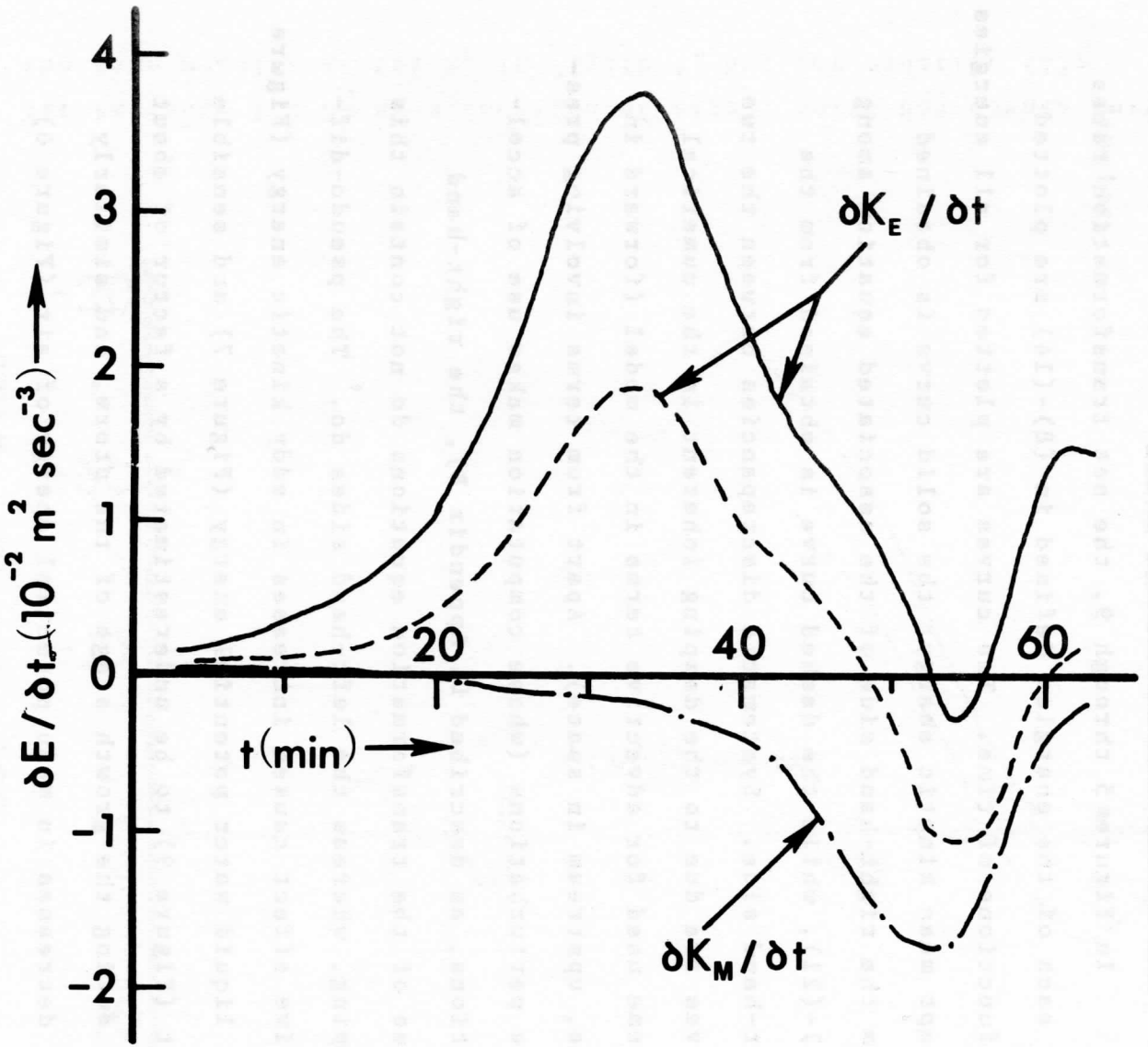

Figure 5. Net tendencies for K_M and K_E as function of time. For K_E, the solid and dashed curves refer to tendencies computed from the right and left sides of equation (16) respectively. Only one curve, obtained from the right side of equation (15), is shown for K_M since the tendencies computed from both sides were nearly the same.

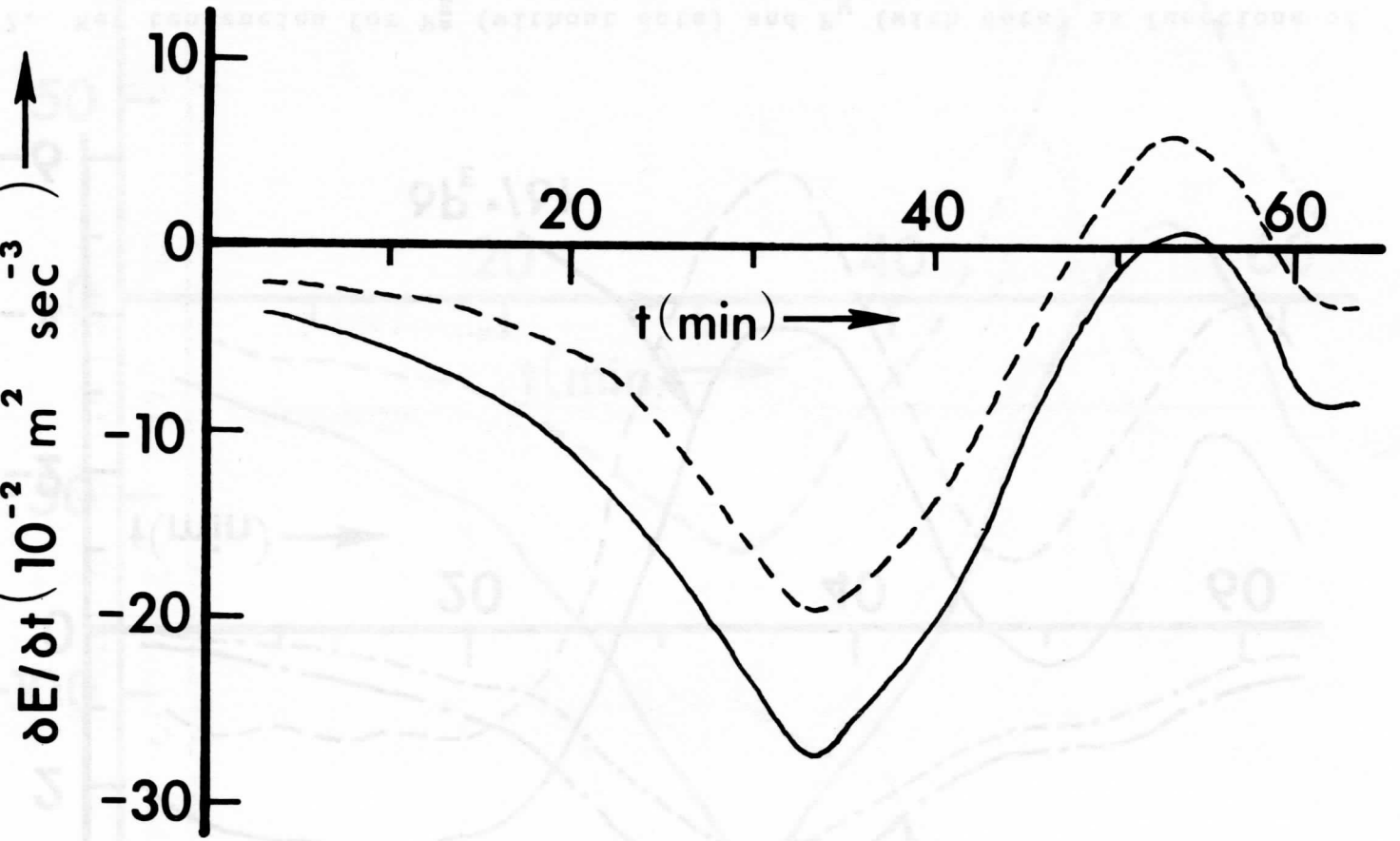

Figure 6. Net tendency for P_M^* as a function of time. Solid and dashed curves have the same meaning as for K_E in Figure 5, but for equation (17).

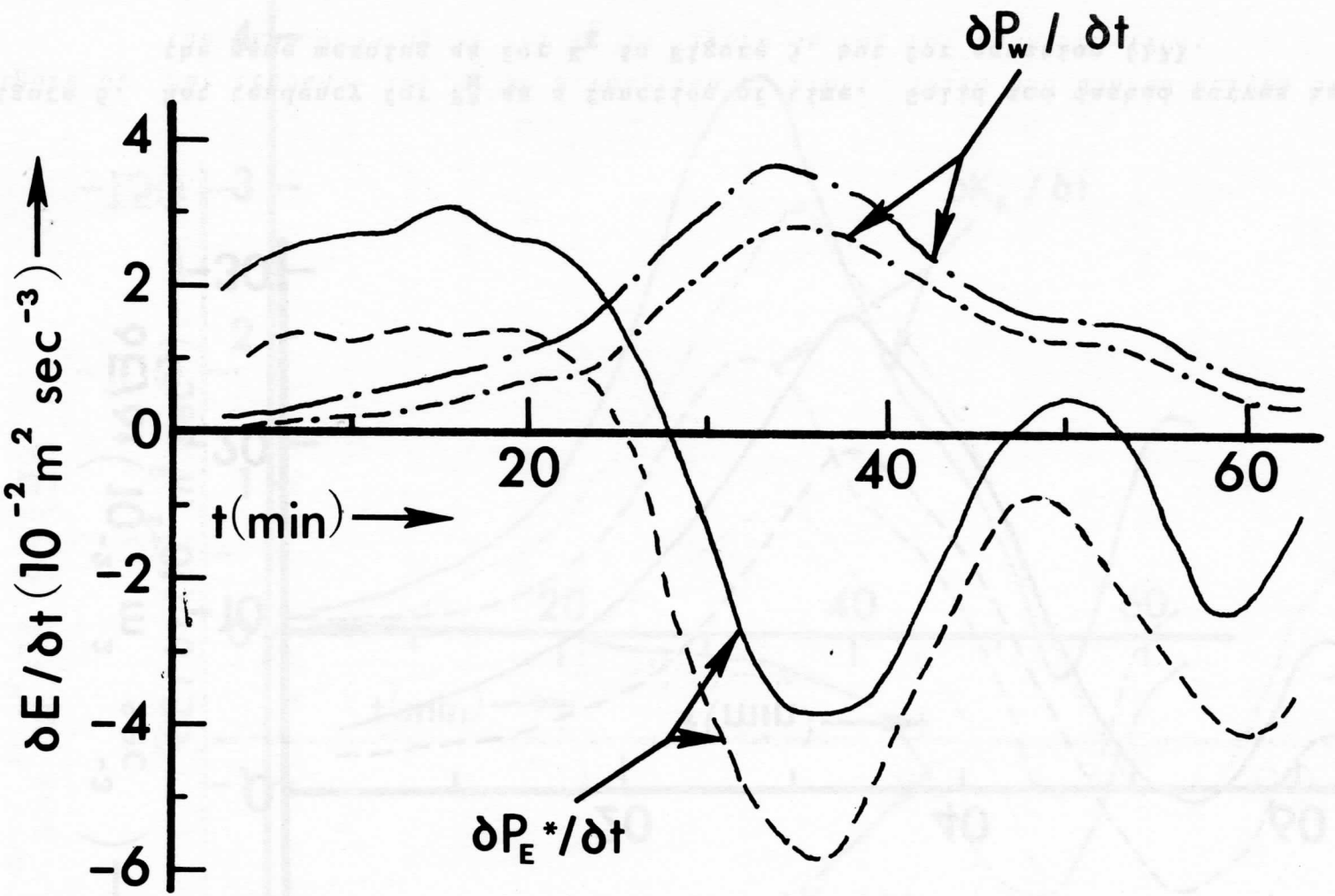

Figure 7. Net tendencies for P_E^* (without dots) and P_W (with dots) as functions of time. Solid and dashed curves have the same meaning as for K_E in Figure 5, but for equations (18) and (19) respectively.

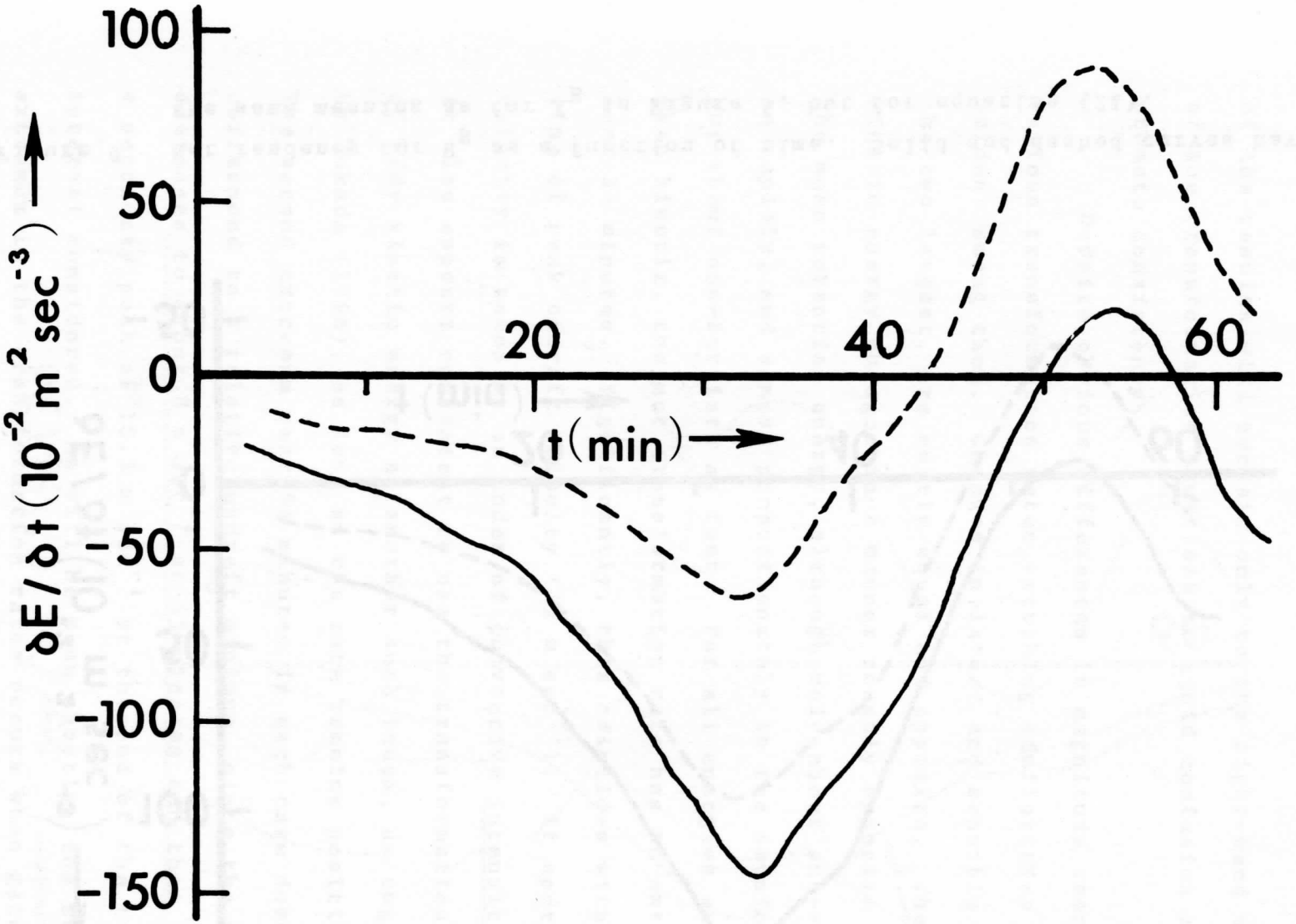

Figure 8. Net tendency for H_L as a function of time. Solid and dashed curves have the same meaning as for K_E in Figure 5, but for equation (20).

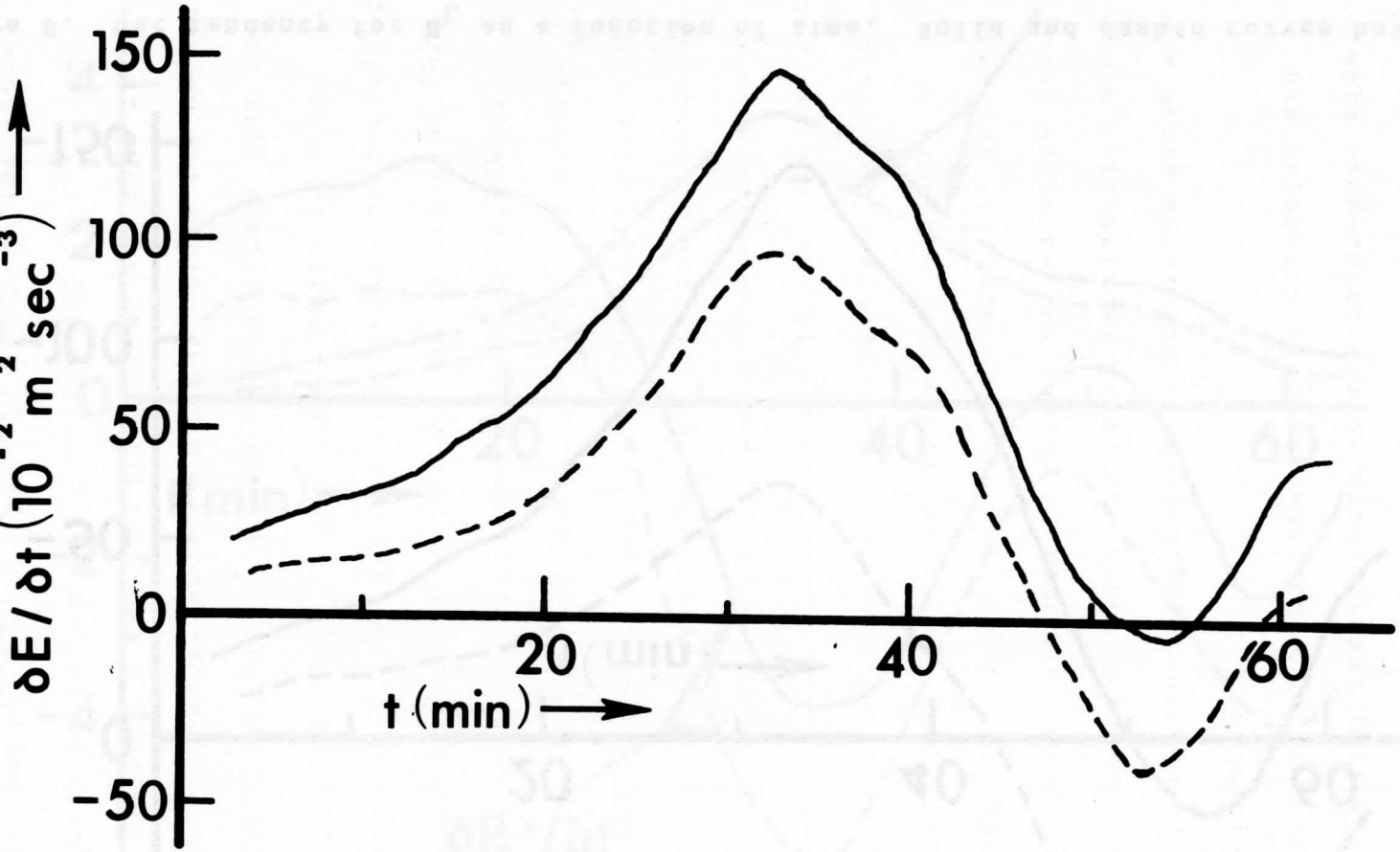

Figure 9. Net tendency for H_S as a function of time. Solid and dashed curves have the same meaning as for K_E in Figure 5, but for equation (21).

of the results will pertain only to the right-hand side of the transformation equations to avoid confusion and promote consistency.

Despite obvious differences in magnitude among the various transformation rates, striking similarities are evident among them. Changes in latent and sensible heat, the two largest, are nearly equal and opposite. The eddy kinetic energy changes in a manner roughly opposite to the mean potential energy, although only about one-sixth as rapidly, and almost proportionately to the sensible heat but about one-fortieth as fast. For all energies except mean kinetic, the net transformation rate has an extremum near 34 minutes. Significantly, this coincides with the time of peak updraft velocity (12 m sec^{-1}). If updraft velocity is taken as an index of convective <u>intensity</u>, it also appears consistent to use the transformation <u>rate</u> of eddy kinetic energy as another such index, as suggested by Takeda (1966), as long as the rate remains positive. The second extremum near 54 minutes in each case does not correspond to a relative updraft minimum, since the updraft decreases to about 8 m sec^{-1} at 45 minutes and then reaches a secondary peak of 10.5 m sec^{-1} at the end of the time interval considered. As will be seen shortly, the second extremum in the transformation rates occurs when gains or losses due to lateral boundary processes assume their greatest

importance.

b) Contributions of individual physical processes to energy transformations

The individual internal and boundary-related physical processes contributing to net energy transformations have been represented in equations (15)-(21) and defined in Tables 1 and 2. Except for the initial time, the values of the corresponding terms are shown in Table 3 for each stage of cloud development depicted in Figure 1. In the remainder of this section, the highlights of the information contained in Table 3 will be summarized for three main aspects: conversions from one energy to another, other internal processes and finally changes due to interactions between the disturbance and the lateral boundaries.

Conversion terms. Of the four conversion terms noted in Section 2, the conversion of latent to sensible heat (A_{13}) is by far the largest, as might be expected. During the mature stage of the storm, eddy potential energy is converted to eddy kinetic energy (A_3), which is in turn converted to potential energy of liquid water (A_6), but these conversions are only a few percent of A_{13}. The conversion of mean to eddy kinetic energy is three orders of magnitude slower than that from latent to sensible heat.

The conversion of mean to eddy kinetic energy results from the momentum transports noted in Section 4, together

TABLE 3

ENERGY TRANSFORMATION RATES
(10^{-2} m^2 sec^{-3})

t(min)	9.0	18.5	27.5	36.1	45.3	54.4	63.0
A_1	.001	-.018	-.049	-.145	-.090	-.091	-.119
A^1	-.003	-.014	-.050	-.115	-.378	-.672	-.320
B^2	-.007	-.033	-.106	-.255	-1.052	-2.913	-1.171
B_2^1	.050	.073	.094	.229	.551	1.956	1.443
$\partial K_M^2/\partial t$	.042	.008	-.111	-.255	-.969	-1.719	-.167
A_3	.404	1.181	3.952	5.187	3.569	5.379	4.804
A^3	-.002	.008	.061	.056	-.293	-.481	-.553
A^4	.002	-.005	-.041	-.016	.250	.403	.458
$-A^5$	-.102	-.314	-1.108	-2.092	-1.580	-1.635	-1.795
A^6	-.001	.018	.049	.145	.090	.091	.119
B^1	.000	.000	.001	-.002	-.120	-.903	-.336
B_3^4	-.000	-.002	-.011	-.044	-.556	-3.113	-1.217
$\partial K_E^4/\partial t$	.300	.884	2.902	3.234	1.360	-.259	1.479
A_7	-5.92	-10.08	-22.08	-26.34	-11.91	-3.92	-7.99
A_9^7	.41	.70	1.48	1.80	1.28	1.28	1.26
B_5	-.02	-.12	-.08	.04	1.81	3.53	-1.50
$P_M^*/\partial t$	-5.53	-9.50	-20.68	-24.50	-8.82	.88	-8.22
A_8	3.342	4.216	4.277	1.404	1.832	4.041	4.260
$-A_3$	-.404	-1.181	-3.952	-5.187	-3.569	-5.379	-4.804
A_{10}	-.231	-.282	-.279	-.089	.046	-.067	-.052
B_6	-.007	-.037	.019	.069	1.135	.796	-.560
$\partial P_E^*/\partial t$	2.700	2.716	.065	-3.804	-.556	-.609	-1.156
A_{11}	0	0	-.697	-1.416	-1.841	-2.025	-2.279
A_{12}	.300	.684	1.985	2.824	2.184	2.007	1.996
A_6	.102	.314	1.108	2.092	1.580	1.635	1.795
B_7	0	0	0	0	0	-.156	-.831
$\partial P_W/\partial t$	.402	.999	2.396	3.501	1.923	1.461	.682
$-A_{13}$	-32.6	-55.0	-117.1	-142.3	-101.0	-101.4	-99.8
B_8	.3	1.5	5.4	14.4	55.0	119.6	52.5
$\partial H_L/\partial t$	-32.3	-53.5	-111.7	-127.9	-46.0	18.2	-47.2
A_{14}	-1.3	-6.1	-19.1	-45.6	-163.8	-342.3	-233.9
A_{13}	32.6	55.0	117.1	142.3	101.0	101.4	99.8
B_9	1.0	4.9	14.3	32.7	110.6	237.5	176.8
$\partial H_S/\partial t$	32.3	53.8	112.3	129.5	47.8	-3.4	42.7

with the positive vertical shear of the mean wind. The increase of conversion rate between 45.3 and 54.4 minutes may be due to downdraft development as well as updraft regeneration. Note that the eddy component of u is defined (see Appendix A) as the departure from the present horizontal average rather than from the initial base state, unlike in Figures 2-4; the vertical transport of horizontal momentum over the region reduces the mean wind shear between 3 and 9 km by almost half during the 63-minute period. Still, the mid-tropospheric mean wind shear remains markedly positive. The conversion of eddy potential to eddy kinetic energy is due mainly to the large upward transport of both sensible heat (produced by condensation) and water vapor within the storm core, while local warming due to subsidence through the stable layer plays some limited role.

One important effect of precipitation is evident from a comparison of A_3 and $-A_6$ in their effects on the eddy kinetic energy. Through 27.5 minutes, only a few minutes after precipitation commences, the latter term is about one-fourth the former, whereas at later times this ratio is between one-third and one-half. This reflects the considerable increase in maximum liquid water content near 4 km resulting from fallout.

The quasi-steady strength of the mature updraft, despite the pulsation mentioned earlier, is reflected in the variation of all four conversion terms by only about

30 percent during the last 27 minutes. Note especially the nearly constant rate of conversion of latent to sensible heat during the last 18 minutes.

Other internal processes. The instability of the main updraft (A_7) is by far the most important element at all times in decreasing the mean potential energy of air, and second in importance only to processes which change the latent and sensible heat. Note, however, that the magnitude of A_7 is far from quasi-steady during the mature stage, unlike the conversion terms, and diminishes greatly between 36.1 and 54.4 minutes. Transient processes well outside the storm core are therefore important in this context. During the growth stage, both the unstable saturated updraft and the stable compensating downdrafts expand greatly both upward and laterally (Figures 2-a and 3-a). Between 36.1 and 54.4 minutes, however, these downdrafts weaken considerably while the broad secondary portion of the splitting updraft seen in Figure 4-a is located almost wholly in stable unsaturated air.

Similar comments apply to A_8, representing the effect of conditional instability upon eddy potential energy of air. The sudden decrease between 27.5 and 36.1 minutes is largely due to transient strong downdrafts in stable air just outside the leading and trailing edges of the cloud; this decrease is the main factor in the change of

net transformation rate from positive to negative. The sharp increase in A_8 from 45.3 to 54.4 minutes reflects both the regeneration of the saturated updraft and the development of part of the cold downdraft in stable air immediately behind the cloud trunk; this air has been humidified, but not saturated, by evaporation.

The very large decrease in sensible heat due to dry-adiabatic temperature changes (A_{14}) reflects the incomplete compensation of updrafts by downdrafts, a situation which of course could not occur in a convective cell with rigid boundaries. The splitting of the primary updraft, together with weak upward motion associated with low-level convergence behind the cold outflow, increase the net dominance of upward motion even as the saturated updraft narrows. Although the term A_2 is not of dominant importance to the marked decrease of mean kinetic energy, its persistently negative sign is associated with the net upward motion over the region; the upward transport of air having relatively low horizontal momentum reduces the mean horizontal wind near 9 km by over 5 m sec^{-1} by the end of the period under study.

Of the three terms (A_9, A_{10} and A_{12}) representing the effect of pseudo-adiabatic condensation or evaporation upon potential energy, only A_{12} is dominant in contributing to net changes. This term represents the increase of liquid

water potential energy due to production of liquid water, and is largely responsible for the persistent increase in this energy. While fallout of precipitation (A_{11}) tends to lower the center of mass of the liquid water, the quasi-steady production of new liquid water above the level of maximum concentration more than balances that effect until the storm is well into the mature stage. Eventually, potential energy loss due to fallout becomes dominant.

The pressure buoyancy (A_4) tends to increase the eddy kinetic energy through 36.1 minutes but then acts to decrease it. High pressure in the upper part of the main updraft is dominant throughout. Meanwhile, as the updraft splits, the leading region of pressure deficit becomes isolated from the saturated updraft as shown in Figure 4-c, reducing the upward pressure buoyancy in the storm core. Note that the compressibility of the atmosphere (A_5), however, strongly counteracts the pressure buoyancy, so that the joint effect of these two contributions is quite small. In an isothermal atmosphere, in fact, these two terms would cancel.

Lateral boundary interactions. Unless otherwise indicated, the remaining discussion will refer to the convection at 54.4 minutes, since it is clear from Table 3 that interactions between the convective disturbance and the lateral boundaries have their greatest importance at

that time.

The dominance of boundary work (B_2) in decreasing the mean kinetic energy is due to the large net pressure decreases from the upshear to the downshear boundary at all levels, (Figure 4-c). Other boundary effects (B_1), including advection, also predominate. The strong horizontal divergence in the outflow from the updraft has created a positive jet downshear and a negative one upshear. As the disturbance propagates downshear and broadens, the positive jet is advected out while the low-momentum upshear current occupies more of the region.

Boundary work (B_4) decreases the eddy kinetic energy sufficiently to counterbalance the increase that updraft regeneration might otherwise produce. The vertical distributions of perturbations in both horizontal velocity and pressure along the downshear boundary are ideal for strong negative boundary work, with pressure excess in the outgoing jet and large pressure deficiency in the low-level inflow. Less important, but still significant, is the negative contribution due to lateral boundary advection (B_3), which is dominated by the exiting of the jet at the downshear boundary.

Both the mean and eddy components of potential energy for air are imported through the boundaries at 54.4 minutes but exported at 63.0 minutes (B_5 and B_6). During

this interval, the mid-tropospheric warming becomes less pronounced along the downshear boundary, where evaporatively cooled air along the underside of the anvil is arriving. At the upshear boundary, simultaneously, the broadening circulation is importing air strongly warmed by previous subsidence. Since the cloud is entirely within the region until about 50 minutes, boundary advection of liquid water (B_7) is of course zero until then, but at 63.0 minutes advection out the downshear boundary contributes sizably to the reduction in potential energy increase for liquid water.

It is interesting to note that at all times shown in Table 3, a net import of both latent and sensible heat (B_8 and B_9) nearly balances the loss of sensible heat due to incompletely compensated upward motion. Throughout the period, this is accomplished by the low-level net convergence produced by the circulation itself. It is thus possible for the net changes in latent and sensible heat to remain nearly equal and opposite, as seen in Figures 8 and 9, despite the importance of boundary interactions at the latest times.

6. FUTURE CONSIDERATIONS

The present two-dimensional numerical model has reproduced some commonly observed thunderstorm phenomena such as mesoscale surface pressure disturbances, heavy rainfall and a quasi-steady storm core during maturity. In particular, as described elsewhere (Schlesinger, 1972), the mature model storm shows the following features:

1) Large-scale entrainment along the cloud boundary at lower and middle levels, as revealed by the horizontal pressure gradient force;

2) Net horizontal convergence up to about 6 km, and divergence at higher levels, in and near the storm core;

3) Almost no variation in the height of the maximum updraft throughout the mature stage, despite somewhat more pronounced time variations in the maximum velocity itself.

Aircraft measurements taken in and near a northeast Colorado hailstorm in July 1971, in the National Hail Research Experiment field program, indicated each of these features to be present. However, there are fundamental limitations inherent in the geometry of the present model, which has attempted to simulate squall-line convection rather than an isolated large cell. Perturbations of wind, and therefore temperature and pressure changes, are exaggerated in the surroundings. Further, certain thunderstorm

phenomena noted in earlier literature or also observed during last summer's NHRE field program cannot be modeled in two dimensions. Most notably,

1) Newton and Newton (1959), Hitschfeld (1960), Goldman (1968) and Fankhauser (1971) have likened a storm core in sheared surroundings to a cylindrical obstacle. Newton and Newton suggested that the three-dimensional distribution of perturbed pressure around the core, as obtained purely by analogy to flow around an obstacle, might perpetuate a storm by contributing to regeneration along its right flank. Not enough observations of perturbed pressure have yet been accumulated to lend concrete support to the obstacle hypothesis, but Fankhauser noted that chaff trajectories at middle and upper levels around an actual storm core over Oklahoma indicated wind speed maxima along the flanks and minima upwind and downwind of the core, implying basic similarities to flow around a cylindrical obstacle. The same characteristics were observed in chaff trajectories near 300 mb around some of last summer's Colorado hailstorms.

2) Browning (1964), Newton (1967) and others have noted that some severe storms propagate to the right of the ambient wind at all levels. For multi-cellular storms, Newton suggested that the dynamic pressure distribution implied by the obstacle analogy might explain this type of propagation, but the situation is not readily explainable

in these terms for large unicellular storms such as Browning emphasized. During the NHRE field program, one storm was observed to travel 50° to the right of the mean wind; in another case, however, a storm split into two echoes, the more persistent one moving to the left of the wind and the less persistent one to the right.

3) At low levels, the NHRE aircraft measurements indicated that the wind around the storm cores did not undergo large perturbations in speed or direction from the upwind to the downwind side. This is in contrast to the present model, which shows surface wind velocity perturbations of some 10 m sec^{-1} well away from the storm core.

While the observed upper wind fields around storm cores appear to corroborate the cylindrical obstacle theory, there are of course no material boundaries separating the storm cores from their surroundings. Accordingly, one might ask why the air within a core might act as a block to the ambient flow. Also, one might ask what dynamical processes not accounted for by the obstacle hypothesis might cause a storm to travel at a large angle to the winds over a deep layer. In this context, the next important step in using numerical models for investigating storm dynamics would appear to be the extension of the present sheared model to three dimensions. While a number of interesting results have been noted in the energetics analysis

summarized in this paper, the restriction to two dimensions has probably caused the importance of lateral boundary interactions to be considerably overestimated. Shafrir et al. (1970) and Fox (1972) have devised three-dimensional numerical models of buoyant convection, including deep moist convection in the first reference; however, no mean wind was assumed, so that phenomena related to shearing or turning of ambient wind with height could not be modeled.

Since the ongoing project is concerned mainly with hailstorms, it might be argued that the most appropriate model should not only be three-dimensional but also include microphysical refinements thus far not used. However, such refinements do not appear essential to investigating phenomena of the type mentioned above. Microphysics has recently been emphasized in one-dimensional models of Weinstein (1970), Danielson et al. (1972) and Kessler and Bumgarner (1971), including freezing in the first two cases.

Even without further refinement of microphysics, incorporating the third dimension will necessitate considerable revision in programming because of the need to go outside of central core memory, and computing time per run will be greatly increased. It appears natural to develop a three-dimensional model in steps such as the following:

1) A dry test model should first be constructed so that certain basic features (such as grid resolution, lateral

boundary conditions or any new advective scheme) can be gauged without requiring the additional computing time and other complications due to moisture. Since there would be four rather than two lateral boundaries, these boundaries might be handled in two steps:

a) Unidirectional basic wind shear parallel to one pair of opposite boundaries can first be assumed. These two boundaries can be treated as walls, possibly taking one of them to be an axis of symmetry (while allowing the development of asymmetry in planes parallel to the basic flow), the other lateral boundaries being open as in the two-dimensional model.

b) Turning of the basic wind with height can then be allowed, making all four lateral boundaries open, in anticipation of using actual wind soundings from past or future NHRE field experiments as initial data after moisture has been incorporated.

2) Once the basic numerics and boundary conditions are deemed satisfactory, moisture can be added to the model. At least temporarily, it may be sufficient to simply extend the present treatment of moisture to three dimensions, deferring further complications that would be entailed in refining the microphysics. Depending on the results of experiments using a fixed grid, it may be advisable to use a suitable extension of the current grid shifting technique.

It should be instructive to use actual NHRE soundings for initial base states (temperature, mixing ratio and wind) as a test of the model's ability to approximate the evolution of actual storms, although some differences are sure to be present until the treatment of microphysics is refined.

APPENDIX A

List of Symbols

x	horizontal co-ordinate
z	vertical co-ordinate
X	length of region
Z	height of region
t	time
c_p	specific heat of dry air at constant pressure ($1.004 \times 10^3 m^2 sec^{-2} C^{-1}$)
g	acceleration of gravity (9.80 m sec^{-2})
γ_d	dry-adiabatic lapse rate, equal to g/c_p (9.77×10^{-3} deg m^{-1})
γ_m	moist-adiabatic lapse rate
Γ	dry-adiabatic lapse rate in unsaturated air, moist-adiabatic lapse rate in saturated air
H_L	latent heat energy of air
H_S	sensible heat energy of air
K_E	eddy kinetic energy of air
K_M	mean kinetic energy of air
L	liquid water content
L_p	precipitation content
L_{vw}	latent heat of vaporization ($2,500 \times 10^6 m^2 sec^{-2}$)
p	pressure
P_E^*	part of eddy potential energy of air (due to temperature and mixing ratio disturbances)
P_M^*	part of mean potential energy of air (due to temperature and mixing ratio disturbances)

P_W potential energy of liquid water

Φ geopotential

Q_0 base state values of a variable Q

$\hat{Q}$ departure of Q from Q_0

$\langle Q \rangle$ mass-weighted area average of Q, $\left(\int_0^X \int_0^Z \rho_0 Q dz dx\right) / \left(\int_0^X \int_0^Z \rho_0 dz dx\right)$

Q'' departure of Q from $\langle Q \rangle$

q_v mixing ratio for water vapor

ρ air density

R_d gas constant for dry air ($2.87 \times 10^2 m^2 sec^{-2} C^{-1}$)

R_v gas constant for water vapor ($4.61 \times 10^2 m^2 sec^{-2} C^{-1}$)

k $(R_v/R_d) - 1$, or approximately 0.61

T temperature

u horizontal velocity of air

$\tilde{u}$ horizontal average of u, $\frac{1}{X} \int_{(0,z)}^{(X,z)} u dx$

$\bar{u}$ mean component of u, defined equal to $\tilde{u}$

u' eddy component of u, defined to be $u - \bar{u}$

w vertical velocity of air

$\tilde{w}$ horizontal average of w, $\frac{1}{X} \int_{(0,z)}^{(X,z)} w dx$

$\bar{w}$ mean component of w, defined equal to 0

w' eddy component of w, defined to be w itself

ψ stream function

S stability parameter, equal to $\dfrac{[\Gamma + \frac{\partial T_0}{\partial z} (1 + \frac{\hat{T}}{T_0})]}{T_0}$

APPENDIX B

Computation of Perturbed Pressure

The pressure disturbance fields shown in Section 4 were obtained by a method whose main steps are outlined below.

1) Equation (2), the vertical equation of motion, is averaged horizontally across all grid rows except the top (z = Z) and bottom (z = 0). Local accelerations and advective terms are computed in terms of first- and second-order derivatives of the stream function ψ with the help of (7). Since forward time differencing is used in the model, this procedure can be carried out at all time steps except the initial one; local accelerations are taken over the preceding time increment, and advective terms are evaluated at the current time step. The horizontal averaging gives a differential equation of form

$$\frac{\partial \tilde{\hat{p}}}{\partial z} + \frac{\tilde{\hat{p}}}{H_0} = F \qquad \text{(B1)}$$

where F is a known function of the wind, temperature and moisture fields, and

$$H_0 = R_d T_0 (1 + k q_{v_0})/g \qquad \text{(B2)}$$

A preliminary solution P_1 is obtained by taking $P_1 = 0$

at $z = \Delta z$, where Δz is the vertical grid separation.

2) Equation (B1) is also satisfied by any function of form $P_1 + ce^{-f(z)}$, where c is a constant and

$$f(z) = \int_{\Delta z}^{z} \frac{ds}{H_0} \tag{B3}$$

In the absence of any obvious physical constraint in addition to consistent values at Δz and $Z - \Delta z$ (which are defined by (B1) itself, creating the indeterminacy just noted), a mathematical constraint is imposed in order to provide a particular solution which avoids unreasonably large horizontally averaged pressure deviations. This solution, P_2, is obtained by requiring that $\int_{\Delta z}^{Z-\Delta z} P_2^2 dz$ be a minimum. The corresponding value c* for c is

$$c^* = -\left(\int_{\Delta z}^{Z-\Delta z} fP_1 dz\right) / \left(\int_{\Delta z}^{Z-\Delta z} f^2 dz\right) \tag{B4}$$

and

$$P_2 = P_1 + c^* e^{-f(z)} \tag{B5}$$

3) Preliminary estimates p_1' for the quantity $(\hat{p} - \tilde{\hat{p}})$ are obtained by setting $p_1' = 0$ at the left boundary and numerically integrating $\partial p_1'/\partial x$ (which is equal to $\partial \hat{p}/\partial x$) to all other points at each level from Δz to $Z - \Delta z$. These values of $\partial \hat{p}/\partial x$ are computed by substitution from the horizontal equation of motion, (1), handling the local acceleration

and advective terms in the same way as for (2) in step 1. Since the horizontal average of $\hat{p}$ is taken to be P_2, we must then have, for $\hat{p}$ at each point,

$$\hat{p} = P_2 + p_1' - \tilde{p}_1'$$

4) Finally, note that the lower boundary (z = 0) and upper boundary (z = Z) are assumed rigid and flat. Boundary conditions for $\hat{p}$ then follow by specializing (2) with both w and $\partial w/\partial x$ zero. Using these conditions and the values of $\hat{p}$ found by step 3 at all points immediately next to the boundaries, one calculates values of $\hat{p}$ along the boundaries.

REFERENCES

Asai, T., 1964: "Cumulus Convection in the Atmosphere with Vertical Wind Shear," J. Met. Soc. Japan, 42, 245-259.

Barnes, S. L., 1970: "Some Aspects of a Severe Right-Moving Thunderstorm Deduced from Mesonetwork Rawinsonde Observations," J. Atmos. Sci., 27, 634-648.

Browning, K. A., 1964: "Airflow and Precipitation Trajectories within Severe Local Storms which Travel to the Right of the Winds," J. Atmos. Sci., 21, 634-639.

Browning, K. A., and R. J. Donaldson, 1963: "Airflow and Structure of a Tornadic Storm," J. Atmos. Sci., 20, 533-545.

Byers, H. R., and R. R. Braham, Jr., 1949: "The Thunderstorm," U.S. Government Printing Office, Washington, D.C., 287 pp.

Danielson, E. F., R. Bleck and D. A. Morris, 1972: "Hail Growth by Stochastic Collection in a Cumulus Model," J. Atmos. Sci., 29, 135-155.

Fankhauser, J. G., 1971: "Thunderstorm-Environment Interactions Determined from Aircraft and Radar Observations," Mon. Wea. Rev., 99, 171-192.

Fox, D. G., 1972: "Numerical Simulation of Three-Dimensional Shape-Preserving Convective Elements," J. Atmos. Sci., 29, 322-341.

Goldman, J. L., 1968: "The High Speed Updraft -- The Key to the Severe Thunderstorm," J. Atmos. Sci., 25, 222-248.

Hitschfeld, W., 1960: "The Motion and Erosion of Convective Storms in Severe Vertical Wind Shear," J. Met., 17, 270-282.

Kessler, E., and W. C. Bumgarner, 1971: "Model of Precipitation and Vertical Air Currents," NOAA Technical Memorandum ERL NSSL-54, National Severe Storms Laboratory, Norman, Oklahoma, 93 pp.

Lettau, H. H., 1967: "New Hypothesis for the Relationship between Eddy and Mean States," Phys. Fluids Supplement, S79-S83.

Newton, C. W., 1967: "Severe Convective Storms," Adv. in Geophys., 12, 257-308.

Newton, C. W., and H. R. Newton, 1959: "Dynamical Interactions between Large Convective Clouds and Environment with Vertical Shear," J. Met., 16, 483-496.

Normand, C. W. B., 1946: "Energy in the Atmosphere," Quart. J. Roy. Met. Soc., 72, 145-167.

Ogura, Y., and J. G. Charney, 1962: "A Numerical Model of Thermal Convection in the Atmosphere," International Symposium on Numerical Weather Prediction, Proc., Tokyo, Japan, Nov. 1960, 431-451.

Schlesinger, R. E., 1972: "A Numerical Model of Deep Moist Convection: The Influence of Ambient Conditions and Internal Physical Mechanisms," Ph.D. thesis, University of Wisconsin, Madison, 339 pp.

Shafrir, U., S. Kaniel and B. Shkoller, 1970: "Three-Dimensional, Time-Dependent Numerical Experiments with Dry and Moist, Shallow and Deep Convection Models," Studies of the Atmosphere Using Aerospace Probings, Annual Report 1969, Space Science and Engineering Center, University of Wisconsin, Madison, 37-87.

Takeda, T., 1965: "The Downdraft in Convective Shower-Cloud under the Vertical Wind Shear and its Significance for the Maintenance of Convective System," J. Met. Soc. Japan, 43, 302-309.

Takeda, T., 1966: "Effects of the Prevailing Wind with Vertical Shear on the Convective Cloud Accompanied with Heavy Rainfall," J. Met. Soc. Japan, 44, 129-143.

Weinstein, A. I., 1970: "A Numerical Model of Cumulus Dynamics and Microphysics," J. Atmos. Sci., 27, 246-255.